Stable high-temperature paramagnons in a three-dimensional antiferromagnet near quantum criticality: Application to $TlCuCl_3$

Maciej Fidrysiak* and Józef Spałek†

Marian Smoluchowski Institute of Physics, Jagiellonian University, ul. Łojasiewicza 11, 30-348 Kraków, Poland

(Received 3 February 2017; published 25 May 2017)

The complete set of hallmarks of the three-dimensional antiferromagnet near the quantum critical point has been recently observed in the spin dimer compound $TlCuCl_3$. Nonetheless, the mechanism, responsible for several distinct features of the experimental data, has remained a puzzle, namely: (i) the paramagnons exhibit remarkable robustness to thermal damping and are stable up to high temperatures, where k_BT is comparable with the excitation energy; and (ii) the width to mass ratios of the high-temperature paramagnons are, within the error bars, equal to that of the low-temperature amplitude (or Higgs) mode. We propose such a mechanism and identify two principal factors contributing to the scaling between width to mass ratios of the paramagnon and the amplitude mode: (i) the emergence of the thermal mass scale reorganizing the paramagnon decay processes, and (ii) substantial renormalization of the multimagnon interactions by thermal fluctuations. The study is carried out for the general case of a $D = 3 + 1$ quantum antiferromagnet within the framework of the φ^4 model using the hybrid Callan-Symanzik + Wilson thermal renormalization group method. Our approach is tested by demonstrating a good quantitative agreement with available experimental data across the phase diagram of $TlCuCl_3$.

DOI: 10.1103/PhysRevB.95.174437

I. INTRODUCTION

The phase diagram of a quantum antiferromagnet in three spatial dimensions involves a quantum critical point (QCP) which separates the Néel phase from the quantum disordered state (QD) at zero temperature [cf. Fig. 1(a)]. Its central part is occupied by the quantum critical (QC) regime, indicating nontrivial interplay between quantum and thermal fluctuations [1]. The transitions between these phases are governed by temperature, as well as by nonthermal parameters that couple to zero-point fluctuations. As one moves along the zero-temperature line, the quasiparticles evolve from the massive excitations in the QD phase to massless spin-wave modes in the Néel state. Additionally, the amplitude (or Higgs) mode, associated with spin fluctuations directed along the ordered moments, is expected on the ordered side of the phase diagram [2]. The recently achieved control of dimerized antiferromagnets $TlCuCl_3$ and $KCuCl_3$ near the pressure-induced quantum phase transition allows for probing all phases depicted in Fig. 1(a) [3–5].

Close to the critical pressure $p_c \approx 1.07$ kbar, stable amplitude modes, characterized by full width at half maximum (FWHM) to mass ratios as low as $\alpha_H \equiv \mathrm{FWHM}_H/m_H \approx 0.2$, have been observed in $TlCuCl_3$ [3,5]. The width to mass ratio of the paramagnons $\alpha_p \equiv \mathrm{FWHM}_p/m_p$ above the Néel temperature T_N turns out to be small in this compound as well. Namely, within the error bars, the equality $\alpha_p(T \gg T_N) \approx \alpha_H(T \ll T_N)$ holds for various values of pressure. In Fig. 1(b) this scaling for $TlCuCl_3$ is depicted along with the straight line $\alpha_p = \alpha_H$ as a guide to the eye. Since the paramagnons have been probed at high temperatures (i.e., for k_BT comparable with the excitation energies), the latter relation implies a remarkably small influence of thermal disorder on broadening of magnetic excitations [6]. In this paper we propose a mechanism protecting the paramagnons from thermal damping and identify two principal factors responsible for the behavior depicted in Fig. 1(b): (i) The emergence of the thermal mass scale $m_T \propto \sqrt{\lambda} \cdot T$, where λ denotes the properly normalized coupling constant (see the discussion below). This particular λ dependence reorganizes perturbation theory in such a way that $\alpha_p(T \gg T_N)$ becomes formally of the same order as $\alpha_H(T \ll T_N)$ and thus allows for the linear scaling between these quantities. (ii) A substantial downward renormalization of λ by thermal fluctuations, which, in turn, leads to reduction of $\alpha_p(T \gg T_N)$. We demonstrate that the latter effect needs to be included to obtain the scaling with the correct proportionality factor.

The study is performed for the general case of a three-dimensional ($D = 3 + 1$) antiferromagnet near the quantum critical point within the framework of the effective φ^4 theory. We employ the hybrid zero-temperature and Wilson thermal renormalization group method that allows us to interpolate between the quantum- and classical-critical behaviors. It is thus suitable for a detailed comparison with experiments on $TlCuCl_3$.

The paper is organized as follows. In Sec. II we derive the widths of magnetic excitations below and above the Néel temperature. In Sec. III we describe the renormalization group procedure. In Sec. IV we propose the mechanism responsible for the scaling between α_p and α_H. Finally, in Sec. V we perform a comparison with the neutron-scattering data on $TlCuCl_3$ across the quantum critical phase diagram. The study is summarized and related to other recent approaches in Sec. VI. The Appendices A–D provide methodological details of the analysis.

*maciej.fidrysiak@uj.edu.pl
†jozef.spalek@uj.edu.pl

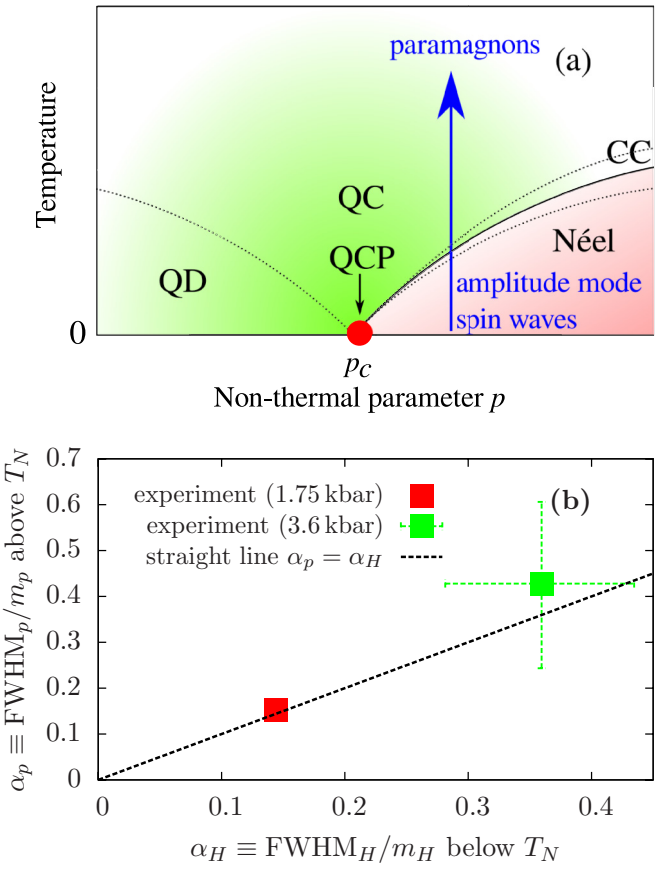

FIG. 1. (a) A schematic phase diagram of a three-dimensional antiferromagnet near the quantum critical point: Néel – antiferromagnetic phase, QD – quantum disordered, QC – quantum critical, CC – classical critical. The dotted lines mark crossovers. As one moves along the vertical arrow, the magnetic excitations evolve from spin waves and the amplitude mode at low-temperature to the high-temperature paramagnons. (b) The scaling between the width to mass ratio for the high-temperature paramagnons and that for the low-temperature amplitude mode. Squares are experimental data of Ref. [5] and the dashed straight line $\alpha_p = \alpha_H$ is a guide to the eye. The high-temperature data have been collected at ∼11.5 and 13 K for $p = 1.75$ and 3.6 kbar, respectively. The low-temperature amplitude mode width to mass ratio has been measured at ∼1.8 K in both cases.

II. φ^4 MODEL AND WIDTH OF THE MAGNETIC EXCITATIONS

We are concerned with the long-wavelength characteristics of magnetic excitations close to the magnetic quantum critical point. In this regime the low-energy physics is expected to be insensitive to the microscopic details of the compound under consideration and can be reliably studied within an effective model approach. Here we employ the φ^4 theory rather than a microscopic spin dimer model, previously applied to $TlCuCl_3$ and $KCuCl_3$ [7]. The magnetic excitations reflect, then, different fluctuation modes of the three-component ($N = 3$) local Néel order parameter $\boldsymbol{\varphi}$ whose dynamics is governed by the Lagrangian

$$\mathcal{L} = \tfrac{1}{2}(\nabla\boldsymbol{\varphi})^2 + \tfrac{1}{2}m^2\boldsymbol{\varphi}^2 + \tfrac{1}{4}\lambda(\boldsymbol{\varphi}^2)^2 + \tfrac{1}{2}\delta m^2\boldsymbol{\varphi}^2 + \tfrac{1}{4}\delta\lambda(\boldsymbol{\varphi}^2)^2. \quad (1)$$

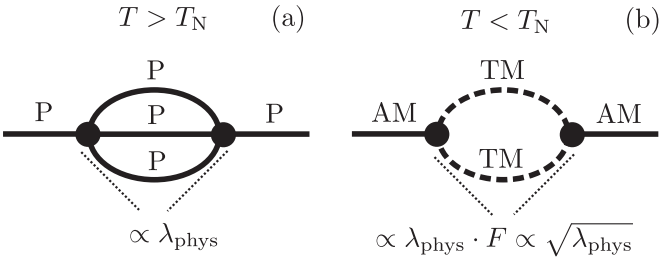

FIG. 2. Leading-order processes yielding broadening of (a) paramagnons above the Néel temperature and (b) amplitude mode below the Néel temperature. Labeling of the lines: P – paramagnon, AM – amplitude mode, TM – transverse mode.

Here m and λ denote the mass parameter and the coupling constant, respectively, whereas δm and $\delta\lambda$ are the counterterms introduced to cancel off the short-wavelength divergences. We work in the natural units by setting to unity the spin-wave velocity ($c = 1$), as well as the Planck's ($\hbar = 1$) and the Boltzmann ($k_B = 1$) constants. Both imaginary time τ and spatial coordinates x, y, z have then the dimension energy^{-1}, mass m, field $\boldsymbol{\varphi}$, and temperature are measured in the units of energy, while λ is dimensionless. The four-gradient symbol then takes the form $\nabla = (\partial_\tau, \partial_x, \partial_y, \partial_z)$.

In the disordered phase, where the physical ("dressed" with quantum and thermal corrections) mass parameter squared m^2_{phys} is positive, all three fluctuation modes of the local order parameter $\boldsymbol{\varphi}$ are equivalent paramagnons of mass $m_p = m_{\mathrm{phys}}$. In this case, the leading-order contribution to broadening of the magnetic excitations (in the sense of perturbative expansion in the effective coupling constant λ_{phys}) comes out directly from the quartic term $\frac{1}{4}\lambda_{\mathrm{phys}} \cdot (\boldsymbol{\varphi}^2)^2$ and is given by the sunset diagram, shown in Fig. 2(a). To derive the explicit form of m^2_{phys} and λ_{phys} one needs to specify the computational scheme, which is detailed below.

In the Néel phase ($m^2_{\mathrm{phys}} < 0$), the order parameter acquires a nonzero expectation value, breaking the spin-rotational symmetry of the system. Without loss of generality one can take $\langle\boldsymbol{\varphi}\rangle = (0, \ldots, 0, F)$, where $F^2 \approx -m^2_{\mathrm{phys}}/\lambda_{\mathrm{phys}}$. As a consequence of symmetry breaking, the longitudinal and transverse fluctuations (defined, respectively, as $\sigma \equiv \varphi^N - F$ and $\pi^i \equiv \varphi^i$ for $i = 1, \ldots, N-1$, with $N = 3$) are no longer equivalent. Also, qualitatively new interactions between σ and $\boldsymbol{\pi}$ emerge, including the three-point vertex $V_{\sigma\boldsymbol{\pi}\boldsymbol{\pi}} = \lambda_{\mathrm{phys}} F \cdot \sigma\boldsymbol{\pi}^2$. The leading-order process contributing to the amplitude mode damping is now generated by $V_{\sigma\boldsymbol{\pi}\boldsymbol{\pi}}$ and is represented by the one-loop diagram shown in Fig. 2(b).

By evaluating the diagrams of Fig. 2 (cf. Appendix A and Ref. [8]), we find the full width to mass ratio of the paramagnon above T_N,

$$\alpha_p \equiv \frac{\mathrm{FWHM}_p}{m_p} = \frac{3\lambda^2_{\mathrm{phys}}(N+2)}{32\pi^3} \cdot \frac{T^2}{m_p^2} \cdot \mathrm{Li}_2(e^{-m_p/T}), \quad (2)$$

and that of the amplitude mode below T_N,

$$\alpha_H \equiv \frac{\mathrm{FWHM}_H}{m_H} = \frac{\lambda_{\mathrm{phys}}(N-1)}{16\pi} \cdot [1 + 2 \cdot n(m_H/2)], \quad (3)$$

respectively. Here $\mathrm{Li}_2(x) = \int_1^x dt\, \frac{\ln(t)}{1-t}$ denotes the dilogarithm.

III. DETERMINATION OF THE EFFECTIVE PARAMETERS

The stability parameters of the paramagnon and the amplitude mode, α_p and α_H [Eqs. (2) and (3)], are formally of different order in the effective coupling constant $\lambda_{\rm phys}$, i.e., $\alpha_p = O(\lambda^2_{\rm phys})$ and $\alpha_H = O(\lambda_{\rm phys})$. The proportionality between α_p and α_H, established experimentally, is hence inconsistent with the casual perturbation theory. Here we perform a nonperturbative resummation of both quantum and thermal fluctuations by the hybrid renormalization group (RG) method, which allows us to track down higher-order effects contributing to the ratio α_p/α_H. Additionally, the latter approach is applicable close both to the quantum and classical transitions and hence provides a unified picture of the quantum critical phase diagram. This property makes it suitable for a global comparison with experiments on dimerized antiferromagnets, where the magnetic excitations have probed in all phases depicted in Fig. 1(a). Here we sketch the derivation of the renormalization group equations and provide the technical details in Appendix B.

The hybrid RG relies on the two scales: (i) renormalization scale μ, introduced by the procedure of subtracting the short-range divergences, and (ii) infrared momentum cutoff to the thermal fluctuations Λ, implemented by redefining the Bose occupation factors $n(E_{\mathbf{k}}) \equiv (\exp(E_{\mathbf{k}}/T)-1)^{-1}$ as $n(E_{\mathbf{k}}) \leftrightarrow n_\Lambda(E_{\mathbf{k}}) \equiv n(E_{\mathbf{k}}) \cdot \theta(|\mathbf{k}|-\Lambda)$, where θ is the Heaviside step function and $E_{\mathbf{k}}$ is the energy of the excitation of wave vector $\mathbf{k}$. In the $\Lambda \to 0$ limit the full factor $n(E)$ is recovered, whereas for $\Lambda \to \infty$ all thermally excited modes are suppressed ($n_{\Lambda\to\infty} = 0$).

The limit $\Lambda \to \infty$ corresponds hence to $T \to 0$, where the scale dependence of the running mass m_μ and the coupling constant λ_μ can be found by solving the $T = 0$ Callan-Symanzik equations:

$$\mu \frac{\partial \lambda_\mu}{\partial \mu} = \frac{2(N+8)}{(4\pi)^2}\lambda_\mu^2, \tag{4}$$

$$\frac{\mu}{m^2}\frac{\partial m_\mu^2}{\partial \mu} = \frac{2(N+2)}{(4\pi)^2}\lambda_\mu. \tag{5}$$

The physically relevant scale is provided by the paramagnon mass in the disordered phase $m_p = m_{\rm phys}$ and by the amplitude mode mass in the Néel state $m_H = (2\cdot|m^2_{\rm phys}|)^{1/2}$. Since Eqs. (4) and (5) describe essentially mean-field behavior with weakly scale-dependent logarithmic corrections, we are allowed to take $\mu = |m^2_{\rm phys}|^{1/2}$ in both phases without imposing significant error so that $m^2_{\rm phys}(T=0) = m^2_\mu\,|_{\mu=\sqrt{|m^2_{\rm phys}|}}$ and $\lambda_{\rm phys}(T=0) = \lambda_\mu\,|_{\mu=\sqrt{|m^2_{\rm phys}|}}$.

Once the zero-temperature parameters are known, the finite-temperature effects can be incorporated by progressively integrating out thermal fluctuations and moving from $\Lambda \to \infty$ to $\Lambda = 0$. The initial conditions at $\Lambda = \infty$ are now given by the physical zero-temperature quantities. This step is equivalent to the Wilson thermal renormalization group method, previously discussed within the real-time [9] and imaginary-time [10] formulation of thermal theory, and leads to the following set of differential equations equations with respect to Λ:

$$\Lambda\frac{d\lambda_\Lambda}{d\Lambda} = (N-1)\lambda_\Lambda^2\mathcal{I}''_\Lambda(m^2_{\perp,\Lambda}) + 9\lambda_\Lambda^2\mathcal{I}''_\Lambda(m^2_{||,\Lambda}), \tag{6}$$

$$\begin{aligned}\Lambda\frac{dm^2_\Lambda}{d\Lambda} =\ & (N-1)\lambda_\Lambda\mathcal{I}'_\Lambda(m^2_{\perp,\Lambda}) + 3\lambda_\Lambda\mathcal{I}'_\Lambda(m^2_{||}) \\ & -(N-1)\lambda_\Lambda^2F_\Lambda^2\mathcal{I}''_\Lambda(m^2_{\perp,\Lambda}) - 9\lambda_\Lambda^2F_\Lambda^2\mathcal{I}''_\Lambda(m^2_{||,\Lambda}),\end{aligned} \tag{7}$$

where $F^2_\Lambda = \max(0, -m^2_\Lambda/\lambda_\Lambda)$ is the square of the antiferromagnetic order parameter, $m^2_{\perp,\Lambda} \equiv m^2_\Lambda + \lambda_\Lambda F^2_\Lambda$, and $m^2_{||,\Lambda} \equiv m^2_\Lambda + 3\lambda_\Lambda F^2_\Lambda$. The temperature enters through the expressions

$$\mathcal{I}'_\Lambda(M^2) = -\frac{\Lambda^3}{2\pi^2}\frac{n(\sqrt{M^2+\Lambda^2})}{\sqrt{M^2+\Lambda^2}}, \tag{8}$$

$$\mathcal{I}''_\Lambda(M^2) = -\frac{\Lambda^3}{2\pi^2}\frac{d}{dM^2}\left[\frac{n(\sqrt{M^2+\Lambda^2})}{\sqrt{M^2+\Lambda^2}}\right]. \tag{9}$$

A supplementary discussion of other variants of the thermal RG equations and the impact of the RG formalism choice on the quantitative discussion of the following sections is provided in Appendix C.

In the next section we analyze the solutions of the above equations to determine the stability of the high-temperature paramagnons.

IV. STABLE HIGH-TEMPERATURE PARAMAGNONS

We now turn to the main result of the paper and explain the relation between $\alpha_p(T \gg T_N)$ and $\alpha_H(T \ll T_N)$. For that purpose, we consider the coupling constant $\lambda_{\rm phys}(T=0)$ as a free variable and calculate both $\alpha_H(T \ll T_N)$ and $\alpha_p(T \gg T_N)$ as a function of $\lambda_{\rm phys}(T=0)$.

The low-temperature amplitude mode stability parameter $\alpha_H(T \ll T_N)$ is uniquely determined by $\lambda_{\rm phys}(T=0)$ through Eq. (3). For $T=0$ we obtain $\alpha_H(T=0) = (N-1)\cdot(16\pi)^{-1}\cdot\lambda_{\rm phys}(T=0)$.

In order to find $\alpha_p(T \gg T_N)$, we need to integrate the thermal RG equations (6) and (7) with the initial conditions $\lambda_{\Lambda=\infty} = \lambda_{\rm phys}(T=0)$ and $m^2_{\Lambda=\infty} = m^2_{\rm phys}(T=0)$. Note that the value of $m^2_{\rm phys}(T=0)$ is irrelevant in the limit $T \to \infty$, where $m^2_{\rm phys}(T=0)/T^2 \to 0$. The high-temperature parameters are hence determined solely by $\lambda_{\rm phys}(T=0)$ and T. In Fig. 3(a) we plot the ratio of the high- to the low-temperature coupling constant as a function of $\log_{10}\lambda_{\rm phys}(T=0)$. In the weak-coupling regime the effects of the thermal flow are negligible; thus $\lambda_{\rm phys}(T=0)$ and $\lambda_{\rm phys}(T \gg T_N)$ can be used interchangeably to formally control the perturbation expansion (although, as we shall show, the flow needs to be included to match the experimental data quantitatively). In Fig. 3(b) the calculated square of the normalized paramagnon mass $m^2_p(T \gg T_N)/T^2$ is shown as a function of the high-temperature coupling constant $\lambda_{\rm phys}(T \gg T_N)$ (black solid line). We observe that $m_p \propto \sqrt{\lambda_{\rm phys}(T \gg T_N)}\cdot T$ for $\lambda_{\rm phys}(T \gg T_N) \ll 1$. In the weak-coupling limit one obtains analytically $m^2_p = (N+2)/12\cdot\lambda_{\rm phys}\cdot T^2$ if the thermal flow of the coupling constant is neglected (red dashed line in Fig. 3). The same analytic expression can be derived by the

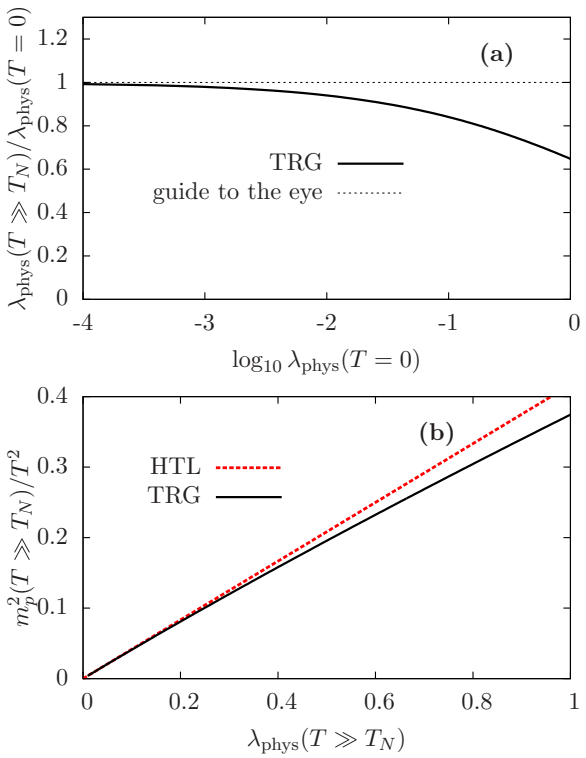

FIG. 3. (a) Ratio of the high- to the low-temperature coupling constants as a function of the low-temperature coupling $\lambda_{\rm phys}(T=0)$. (b) Normalized square of the high-temperature paramagnon mass as a function of the high-temperature coupling constant. TRG – thermal renormalization group. HTL – result of the resummation of the hard thermal loops (see the text).

leading-order diagrammatic resummation of the infinite class of the "hard thermal loops" (HTLs) [8,11], which indicates the nonperturbative origin of the thermal mass. The precise relation of the HTL formalism to the present approach is discussed in Appendix D.

Since the masses appear in the denominators of the magnon propagators, the order of some seemingly subleading diagrams is reduced due to the relation $m_p \propto \sqrt{\lambda_{\rm phys}(T \gg T_N)}$. The latter leads to reorganization of the perturbation expansion so that the width to mass ratio of the paramagnon at high temperatures, given by Eq. (2), now takes the form

$$\alpha_p = \frac{\lambda_{\rm phys}^2(N+2)}{64\pi}\frac{T^2}{m_p^2} + O\left(\lambda_{\rm phys}^{3/2}\ln\lambda_{\rm phys}\right), \qquad (10)$$

where we have made use of the formula $\mathrm{Li}_2(\exp(-x)) = \pi^2/6 + O(x\ln x)$ for $x \to 0$. The first term on the right-hand side of Eq. (10) is $O(\lambda_{\rm phys})$. Since the remainder is of the subleading order $O(\lambda_{\rm phys}^{3/2}\ln\lambda_{\rm phys})$, it should be discarded (otherwise, one would need to include the higher-loop corrections as well for the sake of consistency). The value of $\alpha_p(T \gg T_N)$ can be now obtained by substituting the calculated paramagnon mass $m_p(T \gg T_N) = m_{\rm phys}(T \gg T_N)$ and the coupling constant $\lambda_{\rm phys}(T \gg T_N)$ into Eq. (10). Note that, since we insert the resummed quantities into the perturbative (two-loop) expression, the latter procedure should be viewed as a variation of renormalized perturbation theory and might be not valid arbitrarily close to the classical transition point. The corrections are, however, expected to be logarithmically small in the renormalized mass scale [12,13], and hence we are not concerned with them in the present discussion. It now becomes apparent that, due to the emergence of the thermal mass, $\alpha_p(T \gg T_N)$ is of the same order as $\alpha_H(T \to 0)$, allowing for the linear scaling between these quantities.

The calculated relation between $\alpha_p(T \gg T_N)$ and $\alpha_H(T \ll T_N)$ is depicted in Fig. 4(a) by a black solid line, which is the main result of the paper. In the regime of stable low-temperature amplitude mode ($\alpha_H \lesssim 0.2$), we get $\alpha_p(T \gg T_N) \approx \alpha_H(T \ll T_N)$, in agreement with experiment (the dashed straight line $\alpha_p = \alpha_H$ is a guide to the eye and the solid squares are experimental data for $TlCuCl_3$). The shaded area in Fig. 4(a) is defined by the requirement that the effective zero-temperature quartic coefficient $\lambda_{\rm phys}(T=0)/4$ is smaller than 1, which ensures applicability of the renormalized perturbation theory based on Eqs. (3) and (10). On general grounds, one expects to fall into this regime sufficiently close to the quantum critical point. Indeed, by inspection of the $T=0$ RG equation (4) one can see that, for $m_H \to 0$, $\lambda_{\rm phys}(T=0) \propto 1/\ln(\mu_0/m_H)$, where μ_0 is a (nonuniversal) metric factor. In this limit one hence gets $\lambda_{\rm phys}(T=0) \to 0$ and the computational procedure becomes well controlled.

In Fig. 4(a) we also plot the relation between $\alpha_p(T \gg T_N)$ and $\alpha_H(T \ll T_N)$ calculated with neglected thermal flow of the coupling constant, i.e., $\lambda_{\rm phys}(T=0)$ is used in Eq. (10) instead of $\lambda_{\rm phys}(T \gg T_N)$ (red dot-dashed line). The effect of renormalization of $\lambda_{\rm phys}(T)$ is significant in the experimentally accessed parameter range and must be included to match the data. To further illustrate this point, in Fig. 4(b) we plot the temperature dependence of $\lambda_{\rm phys}(T)/\lambda_{\rm phys}(T=0)$ for the parameters chosen so that $\alpha_H(T=0) = 0.15$. For $T \gg T_N$ (i.e., in the regime most relevant to the present discussion) the coupling constant saturates at the value reduced relative to $\lambda_{\rm phys}(T=0)$. This downward renormalization is reflected in the value of the paramagnon stability parameter $\alpha_p(T \gg T_N)$ and thereby in the proportionality factor between $\alpha_p(T \gg T_N)$ and $\alpha_H(T \ll T_N)$. As one moves towards the Néel temperature, the effects of fluctuations become even more pronounced and $\lambda_{\rm phys}$ approaches zero for $T \to T_N$. The latter behavior is an indirect manifestation of critical slowing down, which requires that the paramagnon decay rate τ_p^{-1} goes to zero as the classical transition is approached [12,14]. Indeed, from the relation $\tau_p^{-1} \propto \mathrm{FWHM}_p$ and Eq. (10) it follows that $\tau_p^{-1} \propto \lambda_{\rm phys}^2(T)/m_p(T)\cdot T^2$. Since the paramagnon gap closes ($m_p \to 0$) for $T \to T_N$, one arrives at $\lambda_{\rm phys} \to 0$ in this limit. Critical slowing down can be also seen directly by plotting the normalized paramagnon width FWHM_p/T vs temperature [black solid line in Fig. 4(c)]. We observe that the calculated FWHM_p/T goes to zero for $T \to T_N$ as anticipated. The solid squares in Fig. 4(c) are experimental values of FWHM_p/T for specific pressure $p = 1.75$ kbar, extracted from Ref. [5]. While the FWHM_p/T at high temperatures exhibits the tendency for saturation, in agreement with thermal RG prediction, there is a qualitative difference near the classical transition as the measured FWHM_p/T increases close to T_N. This point will be addressed in greater detail in the following section.

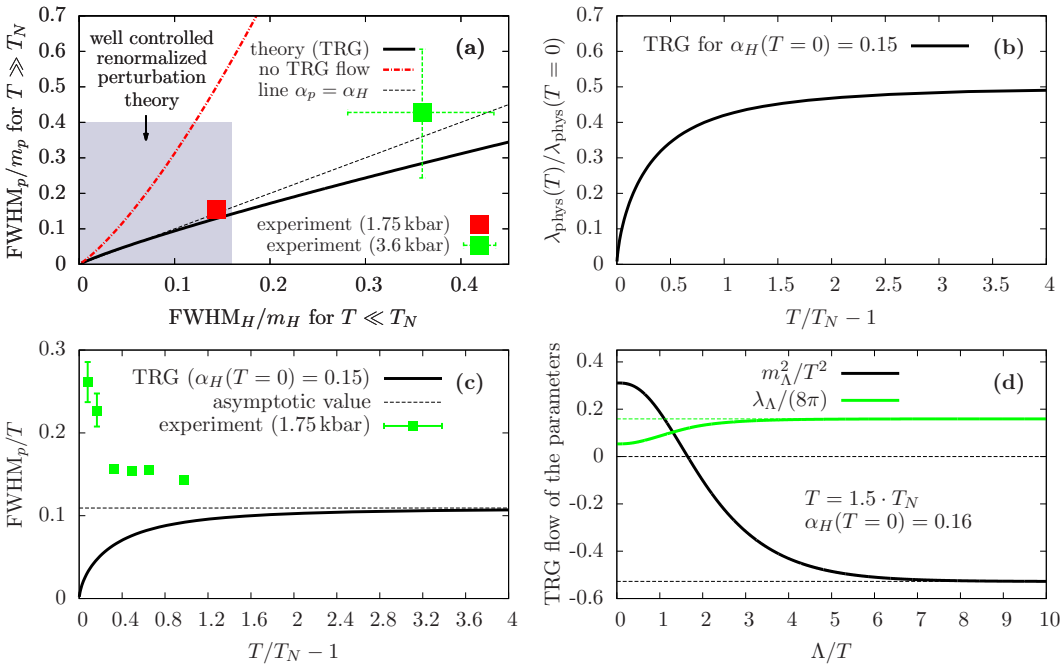

FIG. 4. (a) The relation between the stability parameters of the high-temperature paramagnons and the low-temperature amplitude mode. The black solid line is the solution to the thermal renormalization group (TRG) equations and the dashed line $\alpha_p = \alpha_H$ is a guide to the eye. Solid squares are experimental data of Ref. [5]. The red dot-dashed line shows the relation between $\alpha_p(T \gg T_N)$ and $\alpha_H(T \ll T_N)$ calculated with discarded thermal flow of the coupling constant. The shaded area is defined by the condition $\lambda_{\mathrm{phys}}(T=0)/4 < 1$ that marks the regime of applicability of the renormalized perturbation theory. (b) The ratio of the thermal- to the zero-temperature coupling constant as a function of temperature for the parameters chosen so that $\alpha_H(T=0) = 0.15$. (c) The calculated normalized width FWHM_p/T of the paramagnons as a function of temperature (solid line) for $\alpha_H(T=0) = 0.15$ that roughly corresponds to the experimental value for $TlCuCl_3$ at $p = 1.75$ kbar. The green points are the data extracted from Ref. [5]. (d) Thermal flow of the parameters for $T = 1.5 \cdot T_N$ and $\alpha_H(T=0) = 0.16$. The dashed lines are guides to the eye.

Finally, a typical thermal RG flow of the parameters is depicted in Fig. 4(d). The initial conditions at $\Lambda = \infty$ correspond to the Néel phase ($m^2_{\Lambda=\infty} < 0$). The thermal effects become significant for $\Lambda \approx 3T$ and drive the system to the disordered phase ($m^2_{\Lambda=0} = m^2_{\mathrm{phys}} > 0$) in the physical limit $\Lambda \to 0$.

V. COMPARISON WITH EXPERIMENT: $TlCuCl_3$

In order to make a comparison of the hybrid RG results with the experimental data for the case of a dimerized antiferromagnet $TlCuCl_3$ across the phase diagram, one needs to address relevant material-specific features, such as easy-plane-type magnetic anisotropy $\Delta_{\mathrm{an}} \approx 0.38$ meV, present in this compound. The latter becomes appreciable if some of the paramagnon masses are smaller than Δ_{an}. This happens, e.g., in a narrow slab around the classical transition line, where the anisotropy is expected to induce the crossover from SU(2) to XY behavior. For $TlCuCl_3$ at $p = 1.75$ kbar the above condition is fulfilled for $T/T_N - 1 \approx 0.4$. Remarkably, below this temperature, the experimental FWHM_p/T starts to increase [cf. Fig. 4(c)], which is difficult to reconcile with the anticipated critical slowing down, reproduced by the thermal RG calculation [solid line in Fig. 4(c)]. Similar behavior has been observed in other anisotropic antiferromagnets, e.g., $S = \frac{5}{2}$ MnF_2 and Rb_2MnF_4 [15,16]. From the relations $\mathrm{FWHM}_p/T \propto \lambda^2_{\mathrm{phys}}/m_p \cdot T$ and $\lambda_{\mathrm{phys}} = \lambda_\Lambda\,|_{\Lambda=0}$ one can see that such an upturn of FWHM_p/T is consistent with a partial suppression of the thermal RG flow of λ_Λ below the scale of Δ_{an}. Motivated by this observation, instead of systematic inclusion of the anisotropies as new critical variables, we adopt a heuristic approach and cut off the flow of the coupling constant by taking $\mu = \max(|m^2_{\mathrm{phys}}|^{1/2}, \Delta_{\mathrm{an}})$ as the renormalization scale and performing a shift in the infrared-singular polarization loop contributions to the thermal RG equations [$\mathcal{I}''_\Lambda(M^2) \to \mathcal{I}''_\Lambda(M^2 + \Delta^2_{\mathrm{an}})$ in Eqs. (6) and (7)].

At this point we are fully equipped to make a comparison of the hybrid RG results with experiment and proceed as follows. We define the theory at an arbitrarily chosen scale $\mu_0 = 1$ meV and end up with two free parameters: $m^2_{\mu_0}$ and λ_{μ_0}. Close to the critical pressure, we can further expand $m^2_{\mu_0}(p) = a \cdot (p_c - p)$, where a is a numeric coefficient. The two numbers a and λ_{μ_0} are obtained by fitting to the pressure dependence of the Néel temperature for $TlCuCl_3$ with the result $a = 0.53$ meV^2 kbar^{-1} and $\lambda_{\mu_0} = 7.25$. Note that sizable λ_{μ_0} does *not* control the renormalized perturbation theory. Explicitly, for $\mu_0 = 0.5$ meV we get different values, $\lambda_{\mu_0} = 4.27$ and $a = 0.42$ meV^2 kbar^{-1}, whereas the physical quantities remain unchanged. The actual expansion parameter should be identified either with the coefficient of the φ^4 term in the effective Lagrangian, $1/4 \cdot \lambda_\mu\,|_{\mu=|m_{\mathrm{phys}}|}$ (cf. shaded area in Fig. 4(a)), or with the low-temperature amplitude mode stability parameter, $\alpha_H \approx (8\pi)^{-1} \cdot \lambda_\mu\,|_{\mu=|m_{\mathrm{phys}}|}$, which yields a less stringent criterion. The quality of the fit (blue

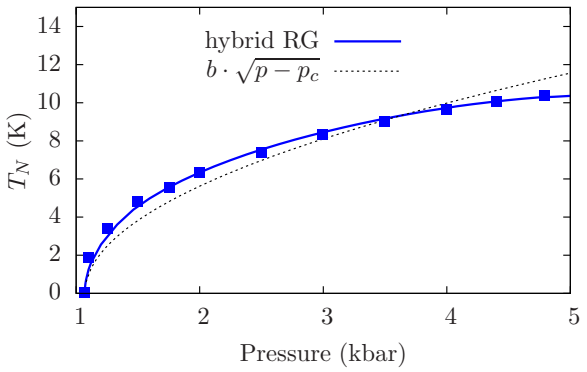

FIG. 5. Fit to the experimental data of Ref. [5]. (solid squares). Blue line – hybrid RG. Black dashed line – fit with a square root form $T_N(p) = b \cdot \sqrt{p - p_c}$.

line in Fig. 5) is remarkable, in contrast to a fit by a simple mean-field form $T_N(p) = b \cdot \sqrt{p - p_c}$ that yields $b \approx 5.83\,\mathrm{K\,kbar}^{-1/2}$ (dotted line). Such a nontrivial pressure dependence of the Néel temperature is likely a manifestation of the logarithmic corrections to scaling at the upper critical dimension, accounted for by the Callan-Symanzik equations [17,18]. With no other fitting parameters, we can now calculate masses and widths of magnetic excitations across quantum and classical transitions by using the RG equations (4)–(5), (6)–(7), combined with Eqs. (3) and (10). The results are confronted with the experimental data of Ref. [5] in Fig. 6.

The temperature dependence of masses of the magnetic excitations for the two selected values of pressure is shown in Fig. 6(a). At low temperatures the data refer to the amplitude mode in the Néel phase, while at high temperatures the data refer to the paramagnon in the disordered state. The transitions between these phases are marked by closing of the gaps at the pressure-dependent Néel temperature $T_N(p)$. The same quantities as a function of pressure for fixed temperature are depicted in Fig. 6(b).

The corresponding width to mass ratios along $T = \text{const.}$ and $p = \text{const.}$ lines are shown in Figs. 6(c) and 6(d), respectively. One can see that the inclusion of the empirical anisotropy scale Δ_{an} has allowed us to reconcile the theoretically predicted critical slowing down with the sharp increase of α_p and α_H close to the Néel temperature. Moreover, the relevance of residual quantum fluctuations (manifested as corrections to the mean scaling at low temperatures) can be inferred from Fig. 6(c). This can be shown by noting that, at the lowest temperatures $T < 2\,\mathrm{K}$, the measured width to mass ratio of the amplitude mode increases by $\sim$100% as the pressure is varied from 1.75 to 3.6 kbar (corresponding to over threefold change of the distance from the quantum critical point $p - p_c$). Since in this temperature range $k_B T$ is by an order of magnitude smaller than the amplitude mode energy [cf. Fig. 6(a)], damping is dominated by the quantum contribution $\alpha_H \approx (N-1)(16\pi)^{-1} \cdot \lambda_{\mathrm{phys}}(T = 0)$. The low-energy behavior of the amplitude mode stability parameter α_H is then controlled by the coupling constant $\lambda_{\mathrm{phys}}(T = 0)$, which is suppressed at a logarithmically slow rate close to the quantum critical point. This relatively weak effect is correctly reproduced by the hybrid RG that also quantitatively agrees with experiment [cf. Fig. 6(c)]. Solving both $T = 0$ RG equations (4)–(5) and thermal RG equations (6)–(7) is hence necessary to match the data across the phase diagram.

Finally, in Figs. 6(e)–6(f) the temperature dependence of the full widths and masses of the magnetic excitations is presented as a function of temperature at the critical pressure $p_c \approx 1.07$ kbar. The hybrid RG solution for the paramagnon mass obeys a linear-T scaling and agrees quantitatively with experiment at low temperatures. The width of the paramagnon, however, deviates from linear T dependence and exhibits a hump close to $T = 4\,\mathrm{K}$. We attribute this behavior to

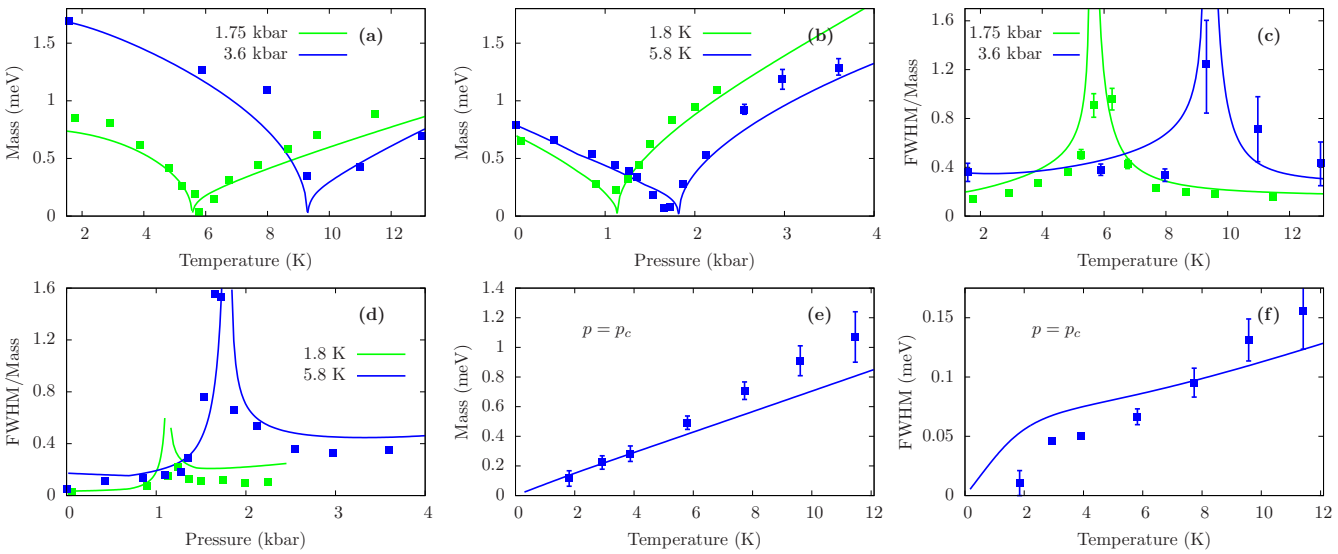

FIG. 6. (a)–(d) Temperature and pressure dependence of masses and widths of the magnetic excitations in $TlCuCl_3$. The curves in the low-temperature regime above $p_c = 1.07$ kbar correspond to the amplitude (Higgs) mode, whereas in the high-temperature and low-pressure range to the paramagnons. (e)–(f) Masses and widths of the magnetic excitations at critical pressure as a function of temperature. In all panels the solid lines are solutions to the hybrid RG equations, while the solid squares are the experimental data of Ref. [5].

the spin anisotropy $\Delta_{\rm an}$, which remains nonzero across the phase transition and becomes comparable with the thermal mass around this temperature. Interestingly, a weak feature can be seen in the experimental data at $\sim$3 K, but detailed analysis cannot be performed due to small numbers of available data points. Worse agreement of the thermal RG result with experiment in Fig. 6(f) relative to Figs. 6(a)–6(e) is likely a consequence of approximate inclusion of magnetic anisotropy in our analysis.

VI. SUMMARY AND DISCUSSION

We have proposed a mechanism leading to a linear scaling (with proportionality factor ≈ 1) between the width to mass ratios of the high-temperature paramagnon and the low-temperature amplitude (Higgs) mode in a dimerized antiferromagnet $TlCuCl_3$, based on: (i) reorganization of the perturbation expansion by the emergence of the thermal mass $\sim\sqrt{\lambda_{\rm phys}}\cdot T$ and (ii) sizable thermal flow of the effective multimagnon coupling $\lambda_{\rm phys}$.

The hybrid Callan-Symanzik + thermal RG approach has allowed us to include both characteristics of the quantum critical point (such as logarithmic suppression of the zero-temperature coupling constant) and the classical critical point (e.g., critical slowing down close to the classical transition). These aspects of the hybrid RG approach, after inclusion of the empirical anisotropy scale, have made it possible to perform a successful comparison with experimental data for $TlCuCl_3$ across the phase diagram in the pressure-temperature plane.

We now comment on the limits of applicability of the present discussion. From a theoretical point of view, the analysis relies on the proximity to the Gaussian quantum critical point in $D = 4$. The $T = 0$ results are thus universal, with the coupling constant vanishing at the QCP. The thermal RG for the ϕ^4 model, on the other hand, suggests that well above the Néel temperature, the (four-dimensional) coupling constant never becomes larger than its $T = 0$ counterpart [cf. Fig. 4(b)]. Moreover, the excitations have well-defined thermal gaps for $T \gg T_N$, and the problem is not spoiled by a singular infrared behavior. The results of the renormalized perturbation theory, based on the thermal-RG transformed Lagrangian, hence retain their validity for $T \gg T_N$ and the calculated relation between α_p and α_H should hold. From the model perspective, at least asymptotically close to the QCP, one can thus universally expect $\alpha_p \approx \alpha_H$.

The question as to what materials the analysis should apply to is, however, delicate for the two reasons:

1. The coupling constant λ in $D = 4$ is marginal and vanishes at a logarithmically slow rate as the QCP is approached. For some compounds, λ might then turn out to be large enough to invalidate the discussion in the experimentally accessible parameter range. This can be checked *a posteriori* once the fitting has been performed. The case of $TlCuCl_3$ is special in this respect, since the amplitude mode turns out to be narrow, indicating the weak-coupling regime [understood as $(N-1)/16\pi\cdot\lambda_\mu\,|_{\mu=|m_{\rm phys}|}\ll 1$].

2. At high temperatures, one cannot formally argue about application of the pure φ^4 model to real materials by referring to the critical point proximity as the lowest-energy excitations are gapped by the large thermal mass. Eventually, other degrees of freedom, not included in the φ^4 model, would participate in the excitation spectrum. These could potentially alter the results at the temperature which is material dependent. (An attempt to account for departures from the φ^4 model physics by including selected dimension six operators is proposed in Ref. [19].) As far as $TlCuCl_3$ is concerned, the thermal masses in the disordered phase do not exceed 1 meV, even for k_BT comparable to the $T = 0$ excitation energies [cf. Fig. 6(a)]. This number is small as compared to the dominant microscopic exchange integral $J \approx 5.5$ meV [7], which supports the applicability of the effective φ^4 theory description in the considered temperature range.

In summary, we require that (i) the low-temperature coupling constant of the material is small, and (ii) there exists a window of temperatures between the classical critical region (governed by the Wilson-Fisher fixed point) and the regime, where the effects of non-φ^4 degrees of freedom become substantial.

We have considered performing a similar analysis for $KCuCl_3$, where the amplitude mode has also been observed [4]. Such a study would be interesting as a different parameter regime is realized in the latter system, resulting in a rather broad amplitude mode. However, since the high-temperature paramagnon data are not available for this compound, the results would not be testable at the present time. Moreover, to the best of our knowledge, the magnetic anisotropies that we need in the fitting procedure have not been measured.

At the end, we would like to point out that there exist alternative approaches to damped excitations, implicitly involving resummation of subclasses of higher-order processes. One of them is based on substitution of "dressed", rather than bare, propagators into the expressions for the dynamical structure factors of magnetic modes. This approach has been employed in the context of the longitudinal spin fluctuations in iron pnictides [20] and extended to a dimerized antiferromagnet [21], which yields a good agreement with the experimental data for $TlCuCl_3$ in the disordered phases for $p > p_c$ and $p = 0$ kbar but fails in the intermediate regime $0 < p < p_c$. The hybrid renormalization group, used here, agrees with the data reasonably well in the disordered state for both $p > p_c$ and $0 < p < p_c$ but overestimates FWHM_p for the lowest pressure $p = 0$ kbar at $T = 5.8$ K [cf. Figs. 6(a)–6(d) and the subsequent discussion in Sec. V).

ACKNOWLEDGMENTS

This work was supported by MAESTRO Grant No. DEC-2012/04/A/ST3/00342 from the Narodowe Centrum Nauki (NCN). The authors are grateful to Prof. Assa Auerbach for discussion.

APPENDIX A: WIDTHS OF THE MAGNETIC EXCITATIONS

In this Appendix all the calculations are performed using resummed parameters $m^2_{\rm phys}$ and $\lambda_{\rm phys}$, but we omit the subscripts for brevity.

1. Amplitude mode below T_N

The leading-order process, giving rise to the amplitude mode decay, is given by the diagram of Fig. 2(b), whose

contribution to the mass operator $\Sigma_H(i\omega_n,\mathbf{k})$ reads

$$\Sigma_H = \lambda m_H^2(N-1)\cdot T\sum_m\!\!\!\!\!\!\int \frac{d^3\mathbf{q}}{(2\pi)^3}G_{\mathrm{TM}}(i\omega_{n-m},\mathbf{k}-\mathbf{q}) \times G_{\mathrm{TM}}(i\omega_m,\mathbf{q}), \tag{A1}$$

where $\omega_n = 2\pi n/T$ are bosonic Matsubara frequencies, and $G_{\mathrm{TM}}(i\omega_n,\mathbf{k}) = (\omega_n^2+\mathbf{k}^2)^{-1}$ denotes the propagator of the spin-wave mode.

The imaginary part of the real-time mass operator at the magnetic zone center $\Sigma_H^{''}(E,\mathbf{0})$ can be evaluated by switching to the real-time representation

$$\frac{1}{\omega_n^2+E_{\mathbf{k}}^2} = \int_0^{1/T} d\tau \frac{e^{i\omega_n\tau}}{2E_{\mathbf{k}}}\cdot[e^{\tau E_{\mathbf{k}}}n_{\mathbf{k}} + e^{-\tau E_{\mathbf{k}}}(1+n_{\mathbf{k}})], \tag{A2}$$

and performing analytic continuation $i\omega_n \to E+i\epsilon$ after working out the integrals over τ variables. The full width of the amplitude mode FWHM_H is then evaluated as

$$\begin{aligned}\mathrm{FWHM}_H \equiv \Sigma_H^{''}(m_H,\mathbf{0})/m_H &= \pi\lambda m_H(N-1) \\ &\times \int \frac{d^3\mathbf{q}}{(2\pi)^3}\delta(m_H-2E_{\mathbf{q}})\cdot\frac{1+2n_{\mathbf{q}}}{(2E_{\mathbf{q}})^2} \\ &= \frac{\lambda m_H(N-1)}{16\pi}\cdot[1+2\cdot n(m_H/2)],\end{aligned} \tag{A3}$$

from which Eq. (3) follows.

2. Paramagnons above T_N

The contribution to the paramagnon mass operator from the diagram, shown in Fig. 2(a), is given by

$$\Sigma_p = 2\lambda^2(N+2)\cdot T\sum_m\!\!\!\!\!\!\int \frac{d^3\mathbf{q}_1}{(2\pi)^3}\frac{d^3\mathbf{q}_2}{(2\pi)^3}G_p(i\omega_{n-m},\mathbf{k}-\mathbf{q}_1) \times G_p(i\omega_{m-l},\mathbf{q}_1-\mathbf{q}_2)\cdot G_p(i\omega_l,\mathbf{q}_2), \tag{A4}$$

where $G_p(i\omega_n,\mathbf{k}) = (\omega_n^2+\mathbf{k}^2+m_p^2)^{-1}$. By switching to the real-time representation and performing analytic continuation $i\omega_n \to E+i\epsilon$, we arrive at $\Sigma_p''(E,\mathbf{0}) \equiv \Sigma_p^{(1)''}(E,\mathbf{0}) + \Sigma_p^{(2)''}(E,\mathbf{0})$, where

$$\begin{aligned}\Sigma_p^{(1)''} = 3\int \frac{d^3\mathbf{q}_1}{(2\pi)^3}\frac{d^3\mathbf{q}_2}{(2\pi)^3}\frac{\delta\left(E-E_{\mathbf{q}_1}-E_{\mathbf{q}_1}+E_{\mathbf{q}_1-\mathbf{q}_2}\right)}{\left(2E_{\mathbf{q}_1}\right)\cdot\left(2E_{\mathbf{q}_2}\right)\cdot\left(2E_{\mathbf{q}_1-\mathbf{q}_2}\right)} \\ \times\left[e^{\left(-E_{\mathbf{q}_1}-E_{\mathbf{q}_1}+E_{\mathbf{q}_1-\mathbf{q}_2}\right)/T}-1\right]\cdot\left(1+n_{\mathbf{q}_1}\right) \\ \times\left(1+n_{\mathbf{q}_2}\right)\cdot n_{\mathbf{q}_1-\mathbf{q}_2}\cdot 2\lambda^2(N+2),\end{aligned} \tag{A5}$$

$$\begin{aligned}\Sigma_p^{(2)''} = \int \frac{d^3\mathbf{q}_1}{(2\pi)^3}\frac{d^3\mathbf{q}_2}{(2\pi)^3}\frac{\delta\left(E-E_{\mathbf{q}_1}-E_{\mathbf{q}_1}-E_{\mathbf{q}_1-\mathbf{q}_2}\right)}{\left(2E_{\mathbf{q}_1}\right)\cdot\left(2E_{\mathbf{q}_2}\right)\cdot\left(2E_{\mathbf{q}_1-\mathbf{q}_2}\right)} \\ \times\left[e^{(-E_{\mathbf{q}_1}-E_{\mathbf{q}_1}-E_{\mathbf{q}_1-\mathbf{q}_2})/T}-1\right]\cdot\left(1+n_{\mathbf{q}_1}\right) \\ \times\left(1+n_{\mathbf{q}_2}\right)\cdot\left(1+n_{\mathbf{q}_1-\mathbf{q}_2}\right)\cdot 2\lambda^2(N+2)\end{aligned} \tag{A6}$$

for $E>0$. By inspecting the arguments of the Dirac δ functions in Eqs. (A5)–(A6) one can see that the first term $\Sigma_p^{(1)''}$ involves paramagnons from the thermal bath and hence is nonzero for $E=m_p$, while $\Sigma_p^{(2)''}$ is the three-paramagnon decay process, which vanishes for $E<3m_p$. It is then sufficient to calculate $\Sigma_p^{(1)''}$.

By introducing dimensionless variables $x = E_{\mathbf{q}_1}/T$ and $y = E_{\mathbf{q}_2}/T$ we arrive at the formula

$$\begin{aligned}\Sigma_p^{(1)''}(m_p,\mathbf{0}) &= \frac{3\lambda^2(N+2)}{32\pi^3}\cdot T^2\cdot(1-e^{-m_p/T}) \\ &\times\int_{\frac{m_p}{T}}^{\infty}dx\int_{\frac{m_p}{T}}^{\infty}dy\frac{1}{e^{-x}-1} \\ &\times\frac{1}{e^{-y}-1}\frac{1}{e^{x+y-m_p/T}-1} \\ &= \frac{3\lambda^2(N+2)}{32\pi^3}\cdot T^2\cdot\mathrm{Li}_2(e^{-m_p/T}),\end{aligned} \tag{A7}$$

where $\mathrm{Li}_2(x)$ is the dilogarithm. The full width of the paramagnon then reads $\mathrm{FWHM}_p = \Sigma_p^{(1)''}(m_p,\mathbf{0})/m_p$ and Eq. (2) is thus reproduced.

APPENDIX B: DERIVATION OF THE RG EQUATIONS

We start with the Lagrangian, given by Eq. (1). The model can be discussed in a unified manner both at $T=0$ and $T>0$ in terms of the quantum effective action, which is a generator of the one-particle irreducible vertex functions [22]. At the one-loop level, the latter may be computed by performing the shift $\boldsymbol{\varphi} \to \boldsymbol{\varphi}_{\mathrm{cl}} + \delta\boldsymbol{\varphi}$, where $\boldsymbol{\varphi}_{\mathrm{cl}}$ is the classical field, and integrating out the fluctuations quadratic in $\delta\boldsymbol{\varphi}$. One then obtains

$$\mathcal{S}_{\mathrm{eff}} = \mathcal{S}[\boldsymbol{\varphi}_{\mathrm{cl}}] + \tfrac{1}{2}\mathrm{Tr}\ln\left\{(-\Delta+m^2)\delta^{\alpha\beta} + \lambda\boldsymbol{\varphi}_{\mathrm{cl}}^2[P_{\perp}^{\alpha\beta}+3P_{||}^{\alpha\beta}]\right\}, \tag{B1}$$

where $\mathcal{S}(\boldsymbol{\varphi}_{\mathrm{cl}}) = \int_0^{1/T}d\tau\int d^3x\mathcal{L}(\boldsymbol{\varphi}_{\mathrm{cl}})$, and $P_{||}^{\alpha\beta} = \varphi_{\mathrm{cl}}^{\alpha}\varphi_{\mathrm{cl}}^{\beta}/\boldsymbol{\varphi}_{\mathrm{cl}}^2$, $P_{\perp}^{\alpha\beta} = \delta^{\alpha\beta} - P_{||}^{\alpha\beta}$ are projectors onto the directions parallel and perpendicular to the classical field $\boldsymbol{\varphi}_{\mathrm{cl}}$, respectively. The effective potential for a constant field $\varphi_{\mathrm{cl}}^i = F\delta^{i,N}$ is then given by $\mathcal{V}_{\mathrm{eff}}(F) = \frac{T}{V}\cdot\mathcal{S}_{\mathrm{eff}}(\boldsymbol{\varphi}_{\mathrm{cl}})$, where V is the volume of space.

We identify the physical temperature-dependent mass parameter $m_{\mathrm{phys}}(T)$ and coupling constant $\lambda_{\mathrm{phys}}(T)$ with the proper derivatives of the effective potential, taken at its minimum, i.e.,

$$\begin{aligned}m_{\mathrm{phys}}^2 &= \frac{\partial^2\mathcal{V}_{\mathrm{eff}}}{\partial F^2} - \frac{1}{2}F^2\frac{\partial^4\mathcal{V}_{\mathrm{eff}}}{\partial F^4} \\ &= m^2+\delta m^2+\lambda[(N-1)\mathcal{A}(m^2+\lambda F^2) \\ &+ 3\mathcal{A}(m^2+3\lambda F^2)] - \lambda^2F^2[(N-1)\mathcal{B}(m^2+\lambda F^2) \\ &+ 9\mathcal{B}(m^2+3\lambda F^2)],\end{aligned} \tag{B2}$$

$$\begin{aligned}\lambda_{\mathrm{phys}} = \frac{1}{6}\frac{\partial^4\mathcal{V}_{\mathrm{eff}}}{\partial F^4} &= \lambda+\delta\lambda+\lambda^2[(N-1)\mathcal{B}(m^2+\lambda F^2) \\ &+ 9\mathcal{B}(m^2+3\lambda F^2)],\end{aligned} \tag{B3}$$

where

$$\mathcal{A}(M^2) = \mathcal{A}_0(M^2) + \int_0^{\infty}\frac{dkk^2}{2\pi^2}\frac{n(\sqrt{M^2+k^2})}{\sqrt{M^2+k^2}}, \tag{B4}$$

$$\mathcal{B}(M^2) = \mathcal{B}_0(M^2) + \int_0^{\infty}\frac{dkk^2}{2\pi^2}\frac{d}{dM^2}\frac{n(\sqrt{M^2+k^2})}{\sqrt{M^2+k^2}}, \tag{B5}$$

$$\mathcal{A}_0(M^2) = \mu^{2\epsilon}\int \frac{d^{4-2\epsilon}\mathbf{k}}{(2\pi)^{4-2\epsilon}}\frac{1}{\mathbf{k}^2+M^2} = -\frac{M^2}{(4\pi)^2}\left[\frac{1}{\epsilon}-\gamma+\ln\left(\frac{\mu^2}{M^2}\right) + \ln(4\pi)+1+O(\epsilon)\right], \tag{B6}$$

$$\mathcal{B}_0(M^2) = -\mu^{2\epsilon}\int \frac{d^{4-2\epsilon}\mathbf{k}}{(2\pi)^{4-2\epsilon}}\frac{1}{(\mathbf{k}^2+M^2)^2} = -\frac{1}{(4\pi)^2} \times \left[\frac{1}{\epsilon}-\gamma+\ln\left(\frac{\mu^2}{M^2}\right)+\ln(4\pi)+O(\epsilon)\right], \tag{B7}$$

and $\gamma \approx 0.577\,2$ denotes the Euler's constant. The term $-1/2\cdot F^2\cdot\partial^2\mathcal{V}_{\rm eff}/\partial F^2$ in the definition of $m^2_{\rm phys}$ [Eq. (B2)] is to cancel the trivial shift coming from the quartic interaction $\lambda\boldsymbol{\varphi}^4$ in the ordered phase ($F^2>0$). The integrals $\mathcal{A}(M^2)$ and $\mathcal{B}(M^2)$ [Eqs. (B4) and (B5)] have been split into the zero-temperature parts $\mathcal{A}_0$ and $\mathcal{B}_0$, and finite-temperature remainders. The short-range divergences are contained only in $\mathcal{A}_0$ and $\mathcal{B}_0$ which have been computed by dimensional regularization with $\epsilon = 2-D/2$ and μ being the regularization scale.

To this point, the expressions (B2) and (B3) are equivalent to the environment-dependent resummation scheme, developed in Ref. [23]. In the following sections we describe renormalization group improvement of this procedure.

1. Callan-Symanzik equations

Since at finite temperatures no new divergences are generated, one can first set $T=0$ (or, equivalently, introduce the cutoff to the Bose factors $n(E_{\mathbf{k}})\to n(E_{\mathbf{k}})\times\theta(|\mathbf{k}|-\Lambda)$ and take the limit $\Lambda\to\infty$). The $1/\epsilon$ terms, divergent for $D\to 4$, are now canceled by the counterterms,

$$\frac{\delta m^2}{m^2} = \frac{\lambda(N+2)}{(4\pi)^2}\cdot\left(\frac{1}{\epsilon}-\gamma+\ln(4\pi)+1\right), \tag{B8}$$

$$\delta\lambda = \frac{\lambda^2(N+2)}{(4\pi)^2}\cdot\left(\frac{1}{\epsilon}-\gamma+\ln(4\pi)\right), \tag{B9}$$

so that the limit $\epsilon\to 0$ can be taken. Note that the form of counterterms is the same for $F=0$ (disordered phase) and $F^2>0$ (ordered phase).

For $F=0$ and $T=0$ one arrives then at the simple expressions

$$m^2_{\rm phys} = \frac{d^2\mathcal{V}_{\rm eff}}{dF^2} = m^2 - \frac{2(N+2)\lambda}{(4\pi)^2}\cdot m^2\cdot\ln\left(\frac{\mu}{m}\right), \tag{B10}$$

$$\lambda_{\rm phys} = \frac{1}{6}\frac{\partial^4\mathcal{V}_{\rm eff}}{\partial F^4} = \lambda - \frac{2(N+8)\lambda^2}{(4\pi)^2}\cdot\ln\left(\frac{\mu}{m}\right). \tag{B11}$$

Equations (4) and (5) can now be obtained from the requirement that the bare vertex functions do not depend on the scale μ. Technically it can be achieved by requiring that the total derivative of the right-hand side of Eqs. (B10) and (B11) is zero to the leading order in λ. Moreover, one can also see that $m^2_{\rm phys} = m^2_\mu\,|_{\mu=m_{\rm phys}}$ and $\lambda_{\rm phys}=\lambda_\mu\,|_{\mu=m_{\rm phys}}$.

In the ordered phase the discussion is more subtle, as Eqs. (B2) and (B3) become spoiled by infrared divergences arising from the massless Goldstone modes. This problem can be overcome by noting that the physical parameters, controlling the amplitude mode, are defined by vertex functions at energy scale $E\approx m_H\approx\sqrt{2|m^2_{\rm phys}|}$ rather than at $E=0$, as implicitly encoded in the effective potential. (This issue is not essential in the disordered phase, where the divergences are suppressed by the paramagnon mass.) Taking that into account would effectively cut off the contribution from the Goldstone modes at $E\approx m_H$. Here we adopt the formulas $m^2_{\rm phys}(T=0)=m^2_\mu\,|_{\mu=\sqrt{|m^2_{\rm phys}|}}$ and $\lambda_{\rm phys}(T=0)=\lambda_\mu\,|_{\mu=\sqrt{|m^2_{\rm phys}|}}$ for both ordered and disordered phase.

2. Thermal renormalization group

We now recover the finite-temperature physics by going from $\Lambda=\infty$ to $\Lambda=0$ in the Wilson renormalization group sense. By integrating out thermal fluctuations with wave vectors $|\mathbf{k}|$ in the infinitesimal slabs $(\Lambda,\Lambda+d\Lambda)$ and taking into account the flow of the parameters through the process, from Eqs. (B2)–(B7) we get

$$\lambda_{\Lambda+d\Lambda} = \lambda_\Lambda + (N-1)\cdot\lambda^2_\Lambda\cdot\mathcal{I}''_\Lambda(m^2_{\perp,\Lambda})\cdot\frac{d\Lambda}{\Lambda} + 9\lambda^2_\Lambda\cdot\mathcal{I}''_\Lambda(m^2_{||,\Lambda})\cdot\frac{d\Lambda}{\Lambda}, \tag{B12}$$

and

$$m^2_{\Lambda+d\Lambda} = m^2_\Lambda + (N-1)\lambda_\Lambda\cdot\mathcal{I}'_\Lambda(m^2_{\perp,\Lambda})\cdot\frac{d\Lambda}{\Lambda} + 3\lambda_\Lambda\cdot\mathcal{I}'_\Lambda(m^2_{||,\Lambda})\cdot\frac{d\Lambda}{\Lambda} - 9\lambda^2_\Lambda F^2_\Lambda\cdot\mathcal{I}''_\Lambda(m^2_{||,\Lambda}) \times\frac{d\Lambda}{\Lambda} - (N-1)\lambda^2_\Lambda F^2_\Lambda\cdot\mathcal{I}''_\Lambda(m^2_{\perp,\Lambda})\cdot\frac{d\Lambda}{\Lambda}, \tag{B13}$$

where $\mathcal{I}'_\Lambda$ and $\mathcal{I}''_\Lambda$ are given by Eqs. (8) and (9). Equations (B12)–(D2) can be now transformed into Eqs. (6) and (7).

APPENDIX C: ROBUSTNESS TO THE CHOICE OF THERMAL RG FORMALISM

The thermal RG exists in a number of variants that differ in the manner in which the effective potential is expanded and truncated. One of the relevant questions is how sensitive are the quantitative results (e.g., the solid lines in Fig. 6) to the choice of the formalism, that we briefly address here.

To expose the potential scheme dependence, in Fig. 7 we plot the damping rates $\gamma\equiv{\rm FWHM}_p/2$ and the coupling constant λ, both as a function of temperature for $N=3$, generated by our method, and compare it with the thermal RG variant of Ref. [14], derived within a slightly different truncation scheme. (Note that Ref. [14] is concerned with the $N=1$ theory and a straightforward extension to $N=3$ is needed to make the comparison.) We plot the results for two choices of the $T=0$ coupling constant: $\lambda(T=0)=1.0$ and $\lambda(T=0)=0.01$.

Both quantities agree with each other far away from the classical critical point, whereas the differences appear below $(T-T_N)/T_N\approx 0.001$. Given that the typical Néel temperature scale is $T_N\lesssim 10\,{\rm K}$ for $TlCuCl_3$ (cf. Fig. 5), the

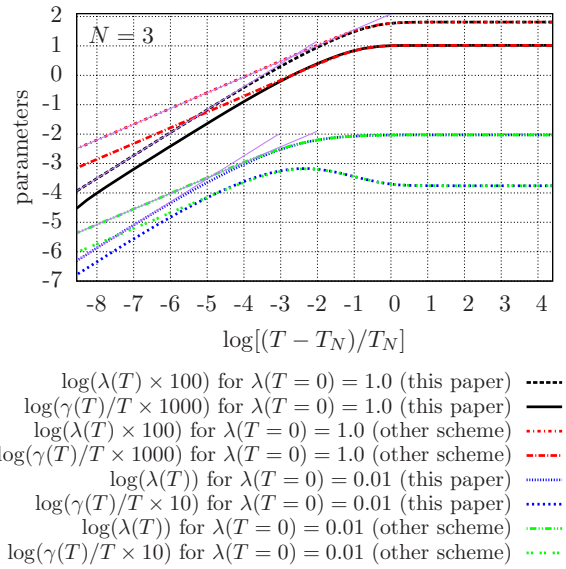

FIG. 7. A comparison of the damping rates $\gamma(T) \equiv \mathrm{FWHM}_p(T)/2$ and the thermal coupling constant $\lambda(T)$ calculated within the formalism of the present paper and the thermal RG variant of Ref. [14] (other scheme). The calculations have been performed for three field components ($N = 3$) and two choices of the zero-temperature coupling constant $\lambda(T = 0) = 1.0$ and $\lambda(T = 0) = 0.01$. The thin purple solid lines are the fits to the curves close to the critical point, as discussed in the text.

two approaches are expected to diverge in a narrow window of ∼0.01 K around T_N. This regime is beyond the reach of current measurements on dimerized magnets and thus is not directly relevant to the present discussion.

The different slopes of the two sets of curves close to T_N, shown in Fig. 7, are by no means unexpected, as they reflect different values of the critical exponents obtained within these approximations. Indeed, both the mass and the coupling constant follow the scaling $m_p(T) \propto t^\nu$ and $\lambda(T) \propto t^\nu$ [12], where $t \equiv (T - T_N)/T_N$ is the reduced temperature. Since, within both schemes, $\gamma \propto \lambda(T)^2/m_p(T) \propto t^\nu$, the damping rate also scales with the same critical index ν.

By performing a linear fit to $\lambda(T)$ for the curves obtained within our scheme, we can extract $\nu = 0.780$ and $\nu = 0.784$ for $\lambda(T = 0) = 1.0$ and $\lambda(T = 0) = 0.01$, respectively. The same procedure for the other scheme yields $\nu = 0.530$ and $\nu = 0.536$. These values are remarkably consistent within each of the approximations, given that the initial coupling constants differ by factor of 100. The thin purple lines in Fig. 7 show the fitted slopes close to T_N. The sensitivity of the estimate for ν to the details of the thermal RG procedure has been noted previously for the case of $N = 1$, where ν varies in the range 0.53–0.689 5 [9].

APPENDIX D: RELATION TO THE HARD THERMAL LOOP FORMALISM

The hard thermal loop formalism is aimed at preserving the consistency of the perturbation expansion at finite temperatures by resummation of the diagrams that otherwise invalidate the perturbation scheme. The latter happens due to

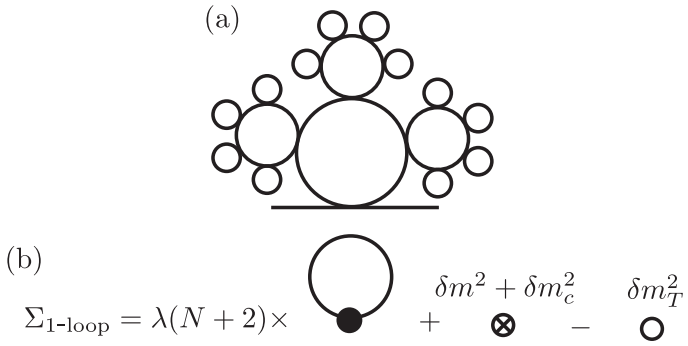

FIG. 8. (a) A representative superdaisy diagram accounted for by resummation. (b) The one-loop contribution to the magnon mass operator in the resummed model.

the emergence of the thermal mass scale $\propto \sqrt{\lambda}$, which changes the order of certain diagrams contributing to the physical quantities (cf. the analysis of Sec. IV). Here we briefly review the HTL approach and discuss its relation to our calculation.

In order to apply the resummation to the φ^4 model, given by Eq. (1), we rewrite it in the following form by adding and subtracting the two terms δm_T^2 and δm_c^2,

$$\begin{aligned}\mathcal{L} = {} & \tfrac{1}{2}(\nabla\boldsymbol{\varphi})^2 + \tfrac{1}{2}m_T^2\boldsymbol{\varphi}^2 + \tfrac{1}{4}\lambda(\boldsymbol{\varphi}^2)^2 \\ & + \tfrac{1}{2}\delta m^2\boldsymbol{\varphi}^2 + \tfrac{1}{4}\delta\lambda(\boldsymbol{\varphi}^2)^2 - \tfrac{1}{2}\delta m_T^2\boldsymbol{\varphi}^2 + \tfrac{1}{2}\delta m_c^2\boldsymbol{\varphi}^2 \\ & - \tfrac{1}{2}\delta m_c^2\boldsymbol{\varphi}^2, \end{aligned} \tag{D1}$$

where $m_T^2 \equiv m^2 + \delta m_T^2$ now has the interpretation of the thermal mass, whereas δm_c^2 is a shift of the mass counterterm that has to be performed [23] to ensure consistency between the resummation and renormalization at each order of the loop expansion. The resummed perturbation theory is implemented by using $G_T(\omega_n,\mathrm{k}) = (\omega_n^2 + \mathbf{k}^2 + m_T^2)^{-1}$ as the three-level propagator and including the terms in the second and the third line of Eq. (D1), starting from the one- and two-loop order, respectively. The optimal δm_T is determined from the requirement that the one-loop correction to the magnon mass vanishes. Physically, in terms of the original propagators $G(\omega_n,\mathrm{k}) = (\omega_n^2 + \mathbf{k}^2 + m^2)^{-1}$, the latter procedure accounts for the resummation of the superdaisy diagrams, whose representative is shown in Fig. 8(a).

The one-loop self-energy, now involving all terms in the second line of Eq. (D1) [cf. Fig. 8(b)], reads

$$\Sigma_{1\text{-loop}} = \lambda(N+2)\mathcal{A}\left(m_T^2\right) + \delta m^2 + \delta m_c^2 - \delta m_T^2, \tag{D2}$$

where $\mathcal{A}(m_T^2)$ is given by Eq. (B5). At high temperatures, the integral on the right-hand side of Eq. (B5) can be evaluated as [24]

$$\begin{aligned}\int_0^\infty \frac{dkk^2}{2\pi^2}\frac{n\left(\sqrt{m_T^2+k^2}\right)}{\sqrt{m_T^2+k^2}} & \\ = \frac{T^2}{12} - \frac{Tm_T}{4\pi} - \frac{m_T^2}{32\pi^2}\left(\ln\frac{m_T^2}{T^2} + 2\gamma - 2\ln(4\pi) - 1\right) & \\ + O\left(\frac{m_T^4}{T^2}\right), & \end{aligned} \tag{D3}$$

which, in conjunction with with Eq. (B6), yields

$$\Sigma_{\text{1-loop}} \approx \lambda(N+2)\left[\frac{T^2}{12} - \frac{T m_T}{4\pi}\right] - \delta m_T^2 - \lambda(N+2)\frac{m_T^2}{32\pi^2}\left(\frac{1}{\epsilon} + \ln\frac{\mu^2}{T^2} + \gamma - \ln(4\pi)\right) + \delta m^2 + \delta m_c^2. \quad \text{(D4)}$$

The necessity of the additional resummation by introducing δm_c^2 becomes apparent now as the coefficient of the $1/\epsilon$ pole involves the thermal mass and is thus temperature dependent. At this point we can cancel the $1/\epsilon$ term by the combined counterterm $\delta m^2 + \delta m_c^2$ to obtain a finite result.

The remaining task is to find δm_T^2 that zeros the self-energy to desired order in λ in the high-temperature limit. To cancel the $O(\lambda)$ terms it is sufficient to take

$$\delta m_T^2 \approx \frac{(N+2)}{12} T^2 \cdot \lambda + O(\lambda^{3/2}). \quad \text{(D5)}$$

Since, for $T \gg T_N$, δm_T^2 dominates the zero-temperature mass, we get $m_T^2 \approx \delta m_T^2 = \lambda(N+2)\cdot T^2/12 + O(\lambda^{3/2})$, in agreement with the analysis of Sec. IV. Note that, in principle, the methodology discussed here could be refined to perform the coupling constant resummation as well. In this Appendix we restrict ourselves to the leading-order expressions and do not track the corrections to λ, which is justified for weak coupling and high temperatures [cf. Fig. 3(a)].

Finally, we show that the expression (D5) is reproduced by the truncated version of the thermal RG equations (6) and (7). To do so, we neglect the thermal flow of λ by discarding Eq. (6). In the high-temperature limit, Eq. (7) can be then recast in the integral form

$$\tilde{m}_{\tilde{\Lambda}}^2 = \frac{(N+2)}{2\pi^2}\int_{\tilde{\Lambda}}^{\infty} \frac{d\tilde{\Lambda}'\tilde{\Lambda}'^2}{\sqrt{\tilde{\Lambda}'^2 + \lambda\tilde{m}_{\tilde{\Lambda}'}^2}} \frac{1}{e^{\sqrt{\tilde{\Lambda}'^2+\lambda\tilde{m}_{\tilde{\Lambda}'}^2}} - 1}, \quad \text{(D6)}$$

where we have switched to the normalized parameters $\tilde{\Lambda} = \Lambda/T$ and $\tilde{m}_{\tilde{\Lambda}} \equiv m_\Lambda/(\sqrt{\lambda}\cdot T)$ and utilized the paramagnetic phase ($F_\Lambda^2 = 0$). Since for $\tilde{m}_{\tilde{\Lambda}}^2 \geqslant 0$ and $\lambda > 0$, the structure of the right-hand side of Eq. (D6) implies that

$$0 \leqslant \tilde{m}_{\tilde{\Lambda}}^2 \leqslant \frac{(N+2)}{2\pi^2}\int_0^{\infty} \frac{\tilde{\Lambda} d\tilde{\Lambda}}{e^{\tilde{\Lambda}} - 1} = \frac{(N+2)}{12} \quad \text{(D7)}$$

and the integrand in Eq. (D6) behaves regularly for $\tilde{\Lambda} > 0$, we can take the $\lambda \to 0$ limit and set $\lambda\tilde{m}_{\tilde{\Lambda}'}^2$ to zero. The weak-coupling solution then reads

$$m_\Lambda^2 = \frac{\lambda T^2(N+2)}{12} - \frac{\lambda T^2}{2\pi^2}\cdot \mathrm{Li}_2(1 - e^{-\Lambda/T}), \quad \text{(D8)}$$

where $\mathrm{Li}_2(x)$ is the dilogarithm. For physical $\Lambda \to 0$ Eq. (D5) is recovered.

[1] S. Chakravarty, B. I. Halperin, and D. R. Nelson, Two-dimensional quantum Heisenberg antiferromagnet at low temperatures, Phys. Rev. B **39**, 2344 (1989).

[2] I. Affleck and G. F. Wellman, Longitudinal modes in quasi-one-dimensional antiferromagnets, Phys. Rev. B **46**, 8934 (1992).

[3] Ch. Rüegg, B. Normand, M. Matsumoto, A. Furrer, D. F. McMorrow, K. W. Krämer, H. U. Güdel, S. N. Gvasaliya, H. Mutka, and M. Boehm, Quantum Magnets Under Pressure: Controlling Elementary Excitations in $TlCuCl_3$, Phys. Rev. Lett. **100**, 205701 (2008).

[4] H. Kuroe, N. Takami, N. Niwa, T. Sekine, M. Matsumoto, F. Yamada, H. Tanaka, and K. Takemura, Longitudinal magnetic excitation in $KCuCl_3$ studied by Raman scattering under hydrostatic pressures, J. Phys.: Conf. Ser. **400**, 032042 (2012).

[5] P. Merchant, B. Normand, K. W. Kramer, M. Boehm, D. F. McMorrow, and Ch. Ruegg, Quantum and classical criticality in a dimerized quantum antiferromagnet, Nat. Phys. **10**, 373 (2014).

[6] O. P. Sushkov, Paramagnons: The long and the short of it, Nat. Phys. **10**, 339 (2014).

[7] M. Matsumoto, B. Normand, T. M. Rice, and M. Sigrist, Field- and pressure-induced magnetic quantum phase transitions in $TlCuCl_3$, Phys. Rev. B **69**, 054423 (2004).

[8] E. Wang and U. Heinz, Plasmon in hot φ^4 theory, Phys. Rev. D **53**, 899 (1996).

[9] M. D'Attanasio and M. Pietroni, Wilson renormalization group formulation of real time thermal field theories, Nucl. Phys. B **472**, 711 (1996).

[10] S.-B. Liao and M. Strickland, Renormalization group approach to field theory at finite temperature, Phys. Rev. D **52**, 3653 (1995).

[11] R. R. Parwani, Resummation in a hot scalar field theory, Phys. Rev. D **45**, 4695 (1992).

[12] M. Pietroni, Plasmon Damping Rate for $T \to T_C$, Phys. Rev. Lett. **81**, 2424 (1998).

[13] B. Bergerhoff and J. Reingruber, A consistent nonperturbative approach to thermal damping-rates, Phys. Lett. B **488**, 435 (2000).

[14] H. Zhang, L. Cheng, and E. Wang, Critical behavior of the damping rate for a plasmon with finite momentum in φ^4 theory, Phys. Rev. D **70**, 037504 (2004).

[15] M. P. Schulhof, R. Nathans, P. Heller, and A. Linz, Inelastic neutron scattering from MnF_2 in the critical region, Phys. Rev. B **4**, 2254 (1971).

[16] K. F. Tseng, T. Keller, A. C. Walters, R. J. Birgeneau, and B. Keimer, Neutron spin-echo study of the critical dynamics of spin-$\frac{5}{2}$ antiferromagnets in two and three dimensions, Phys. Rev. B **94**, 014424 (2016).

[17] H. D. Scammell and O. P. Sushkov, Asymptotic freedom in quantum magnets, Phys. Rev. B **92**, 220401 (2015).

[18] Y. Q. Qin, B. Normand, A. W. Sandvik, and Z. Y. Meng, Multiplicative logarithmic corrections to quantum criticality in three-dimensional dimerized antiferromagnets, Phys. Rev. B **92**, 214401 (2015).

[19] M. S. Chanowitz, New physics and the Landau pole, Phys. Rev. D **63**, 076002 (2001).

[20] M. Fidrysiak, Origin of longitudinal spin excitations in iron-pnictide parent compounds, Eur. Phys. J. B **89**, 41 (2016).

[21] H. D. Scammell and O. P. Sushkov, Nonequilibrium quantum mechanics: A "hot quantum soup" of paramagnons, Phys. Rev. B **95**, 024420 (2017).

[22] C. Itzykson and J.-B. Zuber, *Quantum Field Theory* (McGraw-Hill, Inc., New York, 1980).

[23] A. Jakovác and Zs. Szép, Renormalization and resummation in finite temperature field theories, Phys. Rev. D **71**, 105001 (2005).

[24] L. Dolan and R. Jackiw, Symmetry behavior at finite temperature, Phys. Rev. D **9**, 3320 (1974).